JGR Space Physics

RESEARCH ARTICLE
10.1029/2020JA028388

Comparison of CIMI Simulations and TWINS Observations on June 28 and 29, 2013

Sapna Shekhar[1], J. D. Perez[1], K. Davidson[1,2], and M. C. Fok[3]

[1]Department of Physics, University of Auburn, Auburn, AL, USA, [2]Department of Space Science, University of Alabama in Huntsville, Huntsville, AL, USA, [3]NASA Goddard Space Flight Center, Greenbelt, MD, USA

Key Points:

- Two wide-angle Imaging Neutral-atom Spectrometers (TWINS) global ring current observations and Comprehensive Inner Magnetosphere-Ionosphere (CIMI) simulation results were compared for a moderate geomagnetic storm on June 28 and 29, 2013
- Multiple ion pressure peaks and parallel pressure anisotropies in TWINS data were correlated with substorm ion injections
- During quiet times, effects of shielding electric fields were more prominent in TWINS data than CIMI simulations

Correspondence to:
S. Shekhar,
sap.shekh@gmail.com

Citation:
Shekhar, S., Perez, J. D., Davidson, K., & Fok, M. C. (2021). Comparison of CIMI simulations and TWINS observations on June 28 and 29, 2013. *Journal of Geophysical Research: Space Physics*, *126*, e2020JA028388. https://doi.org/10.1029/2020JA028388

Received 22 JUN 2020
Accepted 12 JUL 2021

Abstract A moderate geomagnetic storm (Sym/H ~−100 nT) during June 28 and 29, 2013 was studied using Comprehensive Inner Magnetosphere-Ionosphere (CIMI) simulations and results were compared with Two wide-angle Imaging Neutral-atom Spectrometers (TWINS) observations of the spatial and temporal evolution of ring current (RC) ions including ion pressure, anisotropy, intensity, and median energy. At the onset of the storm (11:00 UT on June 28), TWINS ion pressure peaks were located radially outward and dusk ward compared to CIMI. During the main phase and the recovery phase (06:00 UT on June 28 to 16:00 UT on June 29), southward IMF *Bz* and rapid AE index fluctuations were observed indicating substorm ion injections and TWINS observed multiple ion pressure peaks at least one of which were found to be close to the locations of CIMI ion pressure peaks. TWINS also observed regions of parallel pressure anisotropy near pre-midnight sectors. The RC ion energies in TWINS were found to be very low (<10 keV) indicating convective transport of O^+ ions. When the storm had nearly recovered post 17:00 UT on June 29, TWINS and CIMI observed single pressure peaks but TWINS ion pressure peaks were radially outward compared to CIMI. Also, the spatial profiles of TWINS ion energies showed gradual removal of low-energy ions. Over all, TWINS and CIMI results were found to agree on the general features of the RC. However, effects of shielding electric fields, particle injections, and presence of O^+ ions were more prominent in TWINS data.

1. Introduction

Earth's inner magnetospheric region is composed of trapped electron and ion populations injected from the magnetotail. The longitudinal drift motion of the ions creates a large-scale current system, known as the ring current (RC). While comparison with in-situ data provides a localized view of the RCs, comparison with RC models like Comprehensive Inner Magnetosphere-Ionosphere (CIMI) (Fok et al., 2014) provide an expanded picture whereby comparisons between the data and simulation lead to an enhanced understanding of the key global processes. The effects of particle injections from the plasma sheet on the formation and decay of RC ions are crucial toward the understanding of RC dynamics.

It is known that the RC pressure exhibits strong asymmetry during the main phase of a storm and in in-situ data and RC models, bulk of the RC pressure has been found to be concentrated in the dusk sector (Anderson et al., 2005; Ebihara et al., 2002; Jorgensen et al., 2004; Le et al., 2004; Shi et al., 2006). However, energetic neutral atom (ENA) images from IMAGE/HENA and Two wide-angle Imaging Neutral-atom Spectrometers (TWINS) have shown that ion fluxes during the main phase of storms may peak near midnight and sometimes near the postmidnight sector (Cson Brandt et al., 2002; Perez et al., 2018). Cson Brandt et al. (2002) proposed shielding electric fields created by the RC and the IMF By effect (twisting of the convection pattern due to By) to explain the eastward skewing of ion intensities. Recently, in a study by Perez et al. (2018), the dynamics of a geomagnetic storm extending through 4 days (September 7–10, 2015) were investigated through comparisons between TWINS data and CIMI model results. General features of the RC were mostly found to be in good agreement, but as expected, consistent indications of enhanced electric shielding and short-time injections from the plasma sheet were not seen in the simulations while they were present in the observations. Further, previous studies such as those by Buzulukova et al. (2010) and Fok et al. (2010) studied the effects of electric shielding on RC morphology through comparisons between in-situ and ENA observations and CIMI simulation results. They found that the eastward skewness of the pressure peak could be explained due to electric shielding effects.

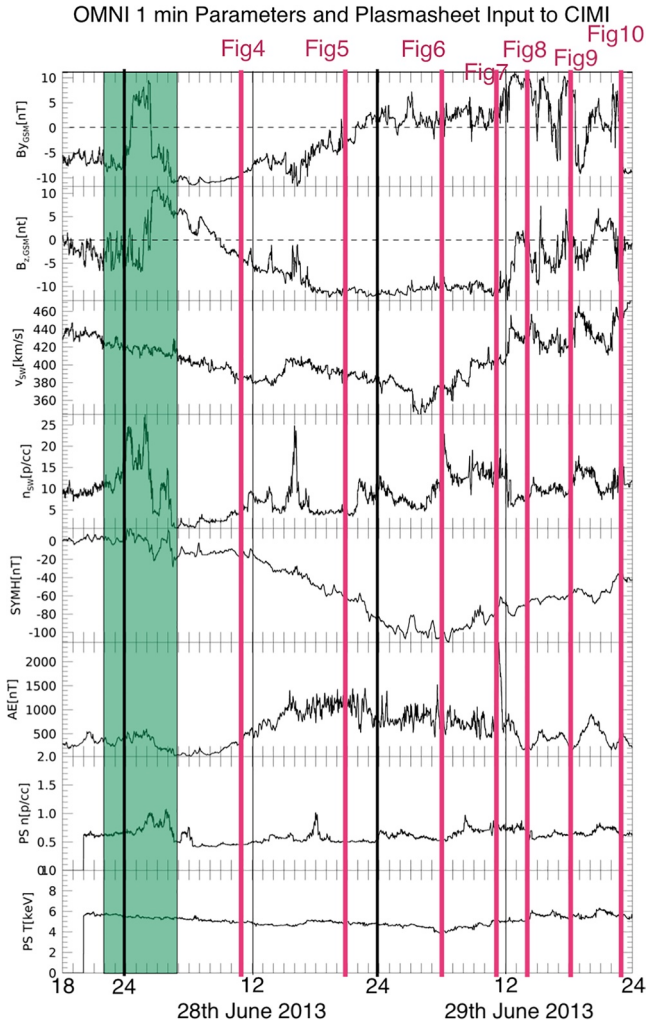

Figure 1. Solar Wind Conditions on June 28 and 29, 2013. IMF *By*, *Bz*, Solar wind speed (v_{SW}), density (n_{SW}), Sym/H, AE index, density (n), and temperature (T) at the plasma sheet are plotted versus time (from top to bottom). The first and the second black vertical lines mark the beginning of June 28 and 29, respectively. In the last two panels, an approximate delay of 2 h is assumed for the solar wind effects to reach the inner plasma sheet. In the highlighted green box, it can be seen that solar wind density (n_{SW}) and IMF *By* have a large peak while the solar wind speed (v_{SW}) is nearly constant. The density peak is followed by rapid northward IMF *Bz* gradually turning southward. This indicates that the geomagnetic disturbance was likely initiated by corotation interaction regions (CIRs). The times where detailed analyses are described in Section 6.1 are marked in red.

Several studies have investigated the role of electric potentials and magnetic fields on the RC dynamics. De Michelis et al. (1999) studied the changes of pressure anisotropy with local time and the noon-midnight pressure asymmetry using 2 years averages of proton distributions measured by (Active Magnetospheric Particle Tracer Explorers) AMPTE/CCE-CHEM (Gloeckler et al., 1985) and correlated them to the current systems out of the equatorial plane completing the closure circuits. They located two different current systems for the quiet period (the RC and the inner portion of the quiet time cross-tail current) and three different current structures for the active period (the RC, the partial RC, and the region 2 current). Kistler and Larson (2000) compared in-situ measurements from AMPTE (Gloeckler et al., 1985) with ion paths obtained from dipole and Tsy04 (Tsyganenko, 1989) magnetic field models with Volland-Stern (Stern, 1975; Volland, 1973) and Weimer96 (Weimer, 1996) electric potential models. They found that the Weimer96 model resulted in better agreement with the features of the ion energy spectra, indicating that in the inner magnetosphere, the electric field may have had a strong influence on particle paths. However, the energies at which closed drift paths were observed were not in agreement with those obtained from simulations. In their analysis, induction electric fields were not included. Angelopoulos et al. (2002) added corotation electric fields and modified Volland-Stern, Weimer96, and Weimer2000 for small-timescale electric field variations from POLAR/HYDRA (Scudder et al., 1995), EQUATOR-S (Kistler et al., 1999), and FAST (Carlson et al., 2001), and found that the simulations showed inconsistencies which could be explained through particle injections and inductive electric fields.

Many features of RC have been studied through CIMI and TWINS comparisons. The first direct comparisons between CIMI (using self-consistent RCM electric field and Weimer2k empirical model) and TWINS ion pressure and anisotropy were made by Perez et al. (2018). Fok et al. (2014) compared CIMI results with TWINS ENA images and Akebono satellites to investigate the dominant energization and loss processes for the RC and radiation belts. Fok et al. (2010) compared CIMI results with TWINS ENA images and in-situ ion data from a THEMIS satellite to study shielding effects. Elfritz et al. (2014) applied TWINS ion temperature boundary conditions to the CIMI model. In this study, we examine the dynamics of global ion spectra and compare the observations with simulation results from the CIMI model during a moderate geomagnetic storm on June 28 and 29, 2013. In Section 2, we describe the evolution of the solar wind conditions during the storm, followed by a description of TWINS image analysis techniques in Section 3, CIMI simulation parameters in Section 4, and calculations of ion pressure, ion pressure anisotropy, and ion spectra in Section 5. In Section 6, we describe the observations and conclusions are discussed in Section 7.

2. Solar Wind Conditions

The 2-day period of the geomagnetic storm (June 28 and 29, 2013) is interesting as the solar wind parameters show both fast and slow variation. Figure 1 shows solar wind conditions from 18:00 UT on June 27 to 00:00 UT on June 30, 2013 (source: omniweb.gsfc.nasa.gov) since the CIMI simulations performed in this study were started at 18:00 UT on June 27. The top six panels show IMF *By*, IMF *Bz*, solar wind speed, density, Sym H, and AE indices, respectively. The bottom two panels show the inputs to the CIMI simulations as described in Section 4. In the highlighted green box, it can be seen that solar wind density (n_{SW}) and IMF *By*

have a large peak while the solar wind speed (v_{SW}) is nearly constant. The density peak is followed by rapid northward IMF *Bz* gradually turning southward. This indicates that the geomagnetic disturbance was likely initiated by corotation interaction regions (CIRs).

On June 28, 2013, between 02:00 and 03:00 UT, IMF *By* and IMF *Bz* changed directions rapidly while the AE index showed little variation. Around noon UT, Sym/H began to gradually dip to negative values and by early morning on June 29, 2013 roughly around 06:30 UT, reached as low as −100 nT. IMF *Bz* remained southward throughout the main phase of the geomagnetic storm. IMF *By* was negative during the onset of the storm but by the end of main phase, gradually shifted to 0 values. During the recovery phase starting at 07:00 UT on June 29 and continuing until the end of the day, IMF *Bz* remained southward and IMF By remained positive. At around 11:00 a.m. on June 29, an isolated large AE peak occurred indicating substorm injections. A couple of hours later, IMF *Bz* fluctuated through negative values as the Sym/H index continued to gradually rise while the AE index showed less variations. The solar wind speed remained nearly constant throughout the storm varying between 360 and 460 km/s.

3. TWINS ENA Images Analysis

NASA TWINS Mission, launched in 2008, enable three-dimensional visualization of the RC dynamics. A pair of identical spacecrafts in two widely separated Molniya orbits with inclinations of 63.4^o, perigee altitudes of ~1,000 km, and apogees in the Northern Hemisphere at ~7.2 RE, each spacecraft is three-axis stabilized and approximately nadir pointing and provide nearly continuous coverage of magnetospheric ENA emissions, over a broad energy range (1–100 keV/amu) with high angular ($4^o \times 4^o$) and temporal (about 1-min) resolution.

To construct a full image, each TWINS instrument has sensor heads that are mounted together on a rotating actuator, which sweeps back and forth, scanning 180^o in 1 min and then taking 22 s to orient in the opposite direction roughly over an Earth-centered viewing cone, scanning 180^o in another 1 min (Goldstein & McComas, 2013). A detailed description of TWINS instruments is given in McComas et al. (2009). The images are integrated over 15–16 sweeps which imply that data is integrated over 15 min over a 20-min time period. Images are enhanced through statistical smoothening and background suppression algorithms (McComas et al., 2012). TWINS measures the time of flight of ENA, thus, from the velocity, the energy/amu can be derived, in the following we will refer simply to energy. ENA images are centered at ion energies ($E_{central}$) from 5 to 65 keV in 5 keV steps (i.e., 13 images). The lower and upper energy range of each data point at a given central energy is given by $[\frac{E_{central}}{2}, \frac{3E_{central}}{2}]$, thus the energy ranges partially overlap to each other. For example, Figures 2a and 2b show global ENA fluxes at a central energy of 10 keV (i.e., flux integrated over energies of 5–15 keV) at 11:00 UT on June 28 and 11:00 UT on June 29, 2013, respectively.

Ion pressure can be extracted from the ENA images from TWINS. For each ENA image, two sources have to be considered. First is the ENAs created by charge exchange of plasma ions with the extended relatively rarefied hydrogen geocorona surrounding the Earth above the ionosphere called high-altitude emissions (HAEs). Second are those created by charge exchange of plasma ions with neutrals in the dense ionosphere, called low-altitude emissions (LAEs). Each pixel in the ENA image represents the number of ENAs per unit time, energy, area, and steradians. The ENAs originating from the geocorona (HAE) can be treated as optically thin while a thick target approximation developed by Bazell et al. (2010) and validated by comparison with DMSP precipitation data is used for the LAE.

For HAE, the value in each pixel in the image array can be expressed as a line-of-sight integration of the ENA intensity in the field-of-view of the pixel defined as the solid angle viewed by the designated pixel (the volume from which the ENAs can enter that pixel of the instrument).

Combining both the contributions from LAE and HAE and then deconvolving the value in the pixel provides ion intensity as a function of three space variables giving the spatial location (three variables) of the source and two angles (two variables) denoting the direction of the velocity of the ENA. However, a line-of-sight integration only contains information about one velocity value in the ion intensity at each spatial point. Hence, the ions are taken to be gyrotropic and assumed to move along magnetic field lines

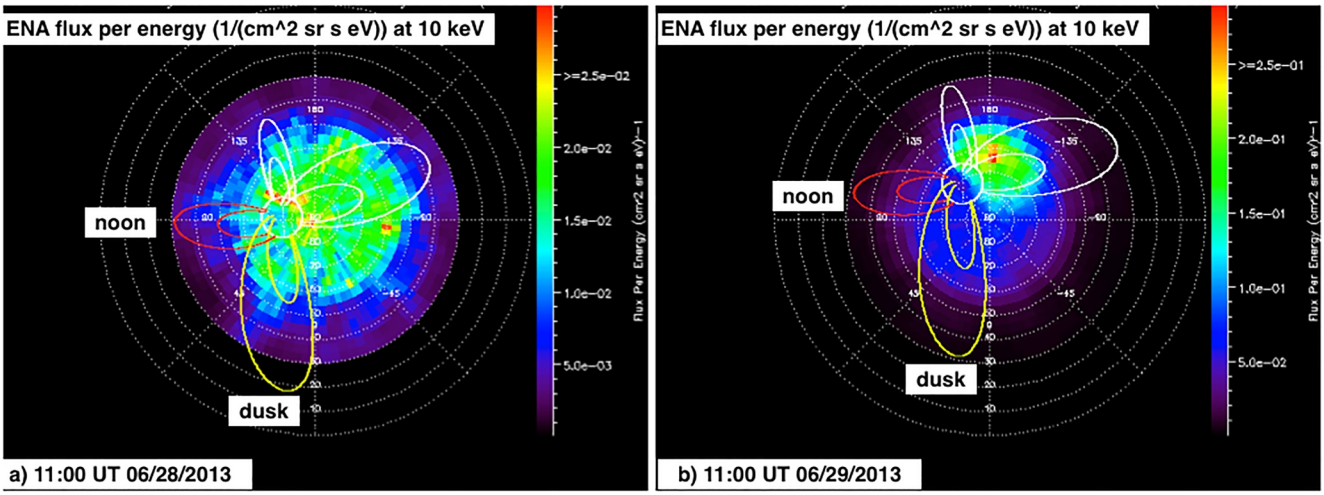

Figure 2. Global energetic neutral atom fluxes from Two wide-angle Imaging Neutral-atom Spectrometers 2 at a central energy of 10 keV (i.e., flux integrated over energies of 5–15 keV) at (a) 11:00 UT on June 28 and (b) 11:00 UT on June 29, 2013. The white circle in the center represents Earth with the magnetic field lines plotted at L shells of 4 and 8. Pink and yellow colors of the magnetic field lines represent noon and dusk magnetic local time sectors, respectively.

conserving their magnetic moments and energies. This allows us to reduce spatial variables to two as each point in three-dimensional space can be mapped to the equator along magnetic field lines using a magnetic field model. Similarly, the pitch angle obtained through constraining the ion to enter the specific pixel can be mapped to the equator. Hence equatorial pitch angle distributions can be extracted. These are then expanded in terms of tri-cubic splines (R & de Boor, 1980). The sum of normalized chi-squared and a penalty function from Wahba (1990) is minimized to fit the data and obtain a smooth solution, respectively. The ion pressure at each spatial point can then be calculated using Equation 1. This is explained in detail in Appendix A of Perez et al. (2012).

From the equatorial ion intensities reconstructed from observed ENA by TWINS at 13 different energies for any spatial point, a singular value decomposition (SVD) fit is obtained. When integrated and properly weighted with the energy-dependent charge exchange cross section, the energy spectrum resembles the SVD fit, is the resulting ion energy spectrum (shown in red in Figure 3). The method is explained in detail in Appendix B of Perez et al. (2012). Hydrogen and Oxygen ENAs can be separated based on mass-dependent differences in the pulse height distributions (Valek et al., 2013). However, deconvolution method can only be applied to the combined ENA to obtain ion spectra for ion energies/atomic mass unit (keV/amu). As such, ion species are not differentiated. In a recent study by Shekhar et al. (2021), TWINS RC ion spectra were compared with RBSP for the main phase of two storms and it was concluded that when O^+ ions were significant, the low energy peaks (<25 keV/amu) in the RC ion spectra were found to be more intense than the high energy peaks (>25 keV/amu). Hence, the energy at the ion spectra peak could be used to infer the nature of the ion species.

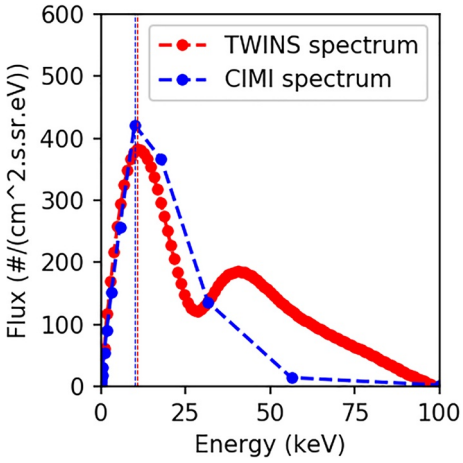

Figure 3. Two wide-angle Imaging Neutral-atom Spectrometers (TWINS) and Comprehensive Inner Magnetosphere-Ionosphere (CIMI) ion spectra at 06:00 UT on June 28 at $L = 3.8$, MLT = 08 h. CIMI flux was readjusted to be comparable with TWINS. TWINS shows two ion flux local maxima and has better energy resolution compared with CIMI since it is obtained as a smooth function through mathematical inversion. The red and blue vertical lines mark the ion energy at the peak of the ion energy spectra for TWINS and CIMI, respectively, in this case ~10–11 keV.

4. The CIMI Model

The CIMI model is a combination of bounce-averaged kinetic model of the RC known as Comprehensive Ring Current Model (CRCM) (Fok et al., 2001) and radiation belt environment (RBE) model (Fok et al., 2008), which also considers charge exchange loss, energy, and pitch-angle diffusion due to whistler-mode chorus waves and plasmaspheric hiss. Details of the model are available in Fok et al. (2014). In this

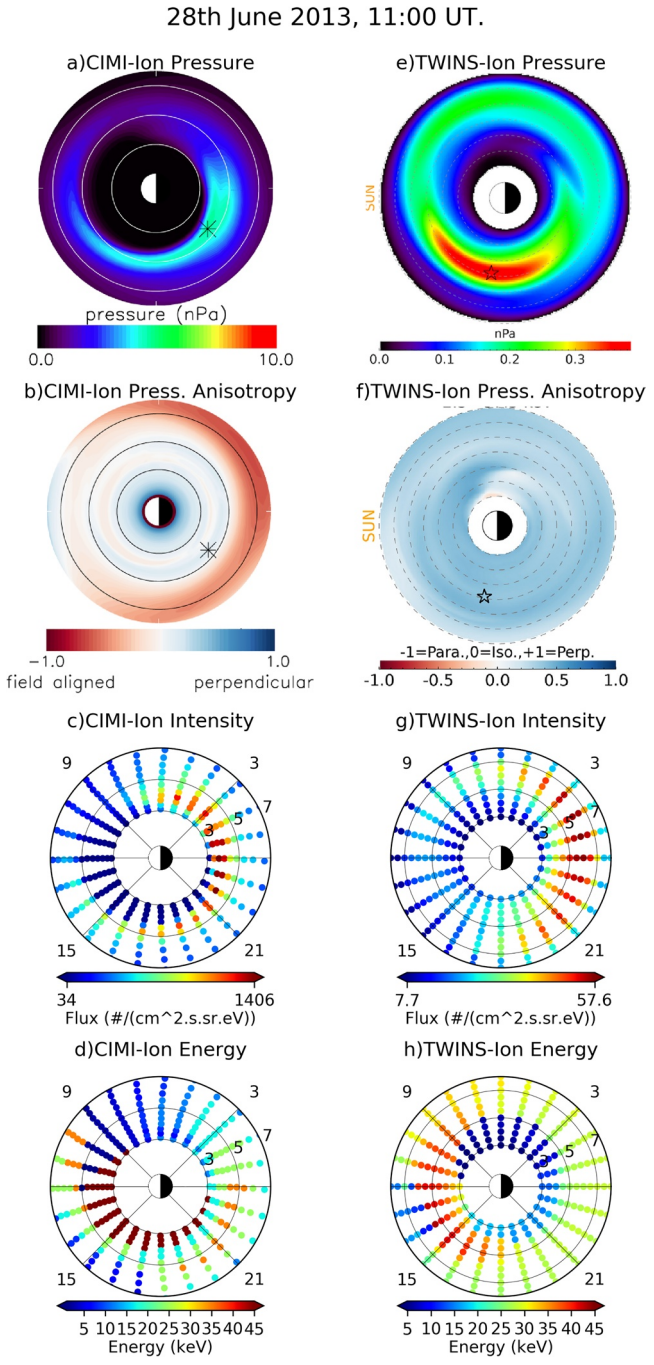

Figure 4. Equatorial profiles of ion pressure, anisotropy, intensity, energies at which intensity peaks were observed are shown from top to bottom at 11:00 UT, June 28, 2013. CIMI simulation results are shown on the left (a–d) while TWINS observations are shown on the right (e–h). The sun is located to the left and the azimuthal coordinates represent MLT. The radial coordinates represent the radial locations mapped to SM equator. Location of maximum ion pressure is marked with black star in TWINS and black asterisk in CIMI. In a and b the concentric radial circles mark radial locations of $3R_E$, $5R_E$ and $7R_E$. The ion intensities and ion energies refer to the peaks in RC ion intensities and related energy in the spectra, as shown in Figure 3.

study, Fok kinetic model solves the bounce averaged Boltzmann equation with a self-consistent Rice Convection Model (RCM) (Harel et al., 1981) electric field. The Hardy model (Hardy et al., 1987) provides auroral conductance which is used for the RCM calculation of the electric field. The electron precipitation is also used to modify the ionosphere conductance and thus the convection potential calculation.

In this study, CIMI simulations were performed for the geomagnetic conditions on June 28 and 29, 2013 to compare the spatial profiles of ion pressures, anisotropies, ion intensities, and peak energies. The RC is assumed to be comprised of H^+ ions. The simulation was started 5 h before 00:00 UT on June 28, 2013. The distribution of the incoming particles injected into the inner magnetosphere along the outer boundary of the simulation ($\sim 10R_E$) is taken to be isotropic, Maxwellian, and uniform over local time with density (n) and temperature (T) (Fok et al., 2003) at any given time t determined by a linear relationship to the solar wind density (n_{SW}) and velocity (v_{SW}), respectively (Borovsky et al., 1998; Ebihara & Ejiri, 2000) given by:

$$n(t)[cm^{-3}] = 0.395 + 0.025 n_{SW}(t - delay)$$
$$T(t)[keV] = -3 + 0.03 v_{SW}(t - delay)$$

where delay (taken to be 2 h in this study) is an approximation of the time for the solar wind effects to reach the inner plasma sheet from locations of Ace and Wind at L1 where the solar wind parameters are observed. The convection electric field starts to trigger the storm just after. These quantities are plotted in the bottom two panels of Figure 1. It is to be noted that the input from the plasma sheet is relatively smooth. Thus, differences in comparison with TWINS observations emphasize the effects of time-dependent and spatial-dependent injections into the inner magnetosphere.

5. Calculations of Ion Pressure, Anisotropy, and Energy Spectrum

The ion pressure at each spatial point is calculated as given in Equation 1.

$$P = \frac{4\pi}{3} \int_{E_1}^{E_2} dE \sqrt{2mE} \int_{-1}^{1} F(E, n, cos\alpha) dcos\alpha (1 + cos^2\alpha) \quad (1)$$

Where α is the ion pitch angle, E is the ion energy, n is the ion density, m is the ion mass and $F(E, n, \cos\alpha)$ is the number flux per unit area, energy, time, and steradian. The CIMI ion pressure in this study are calculated over an energy range of $E_1 = 1$ to $E_2 = 121$ keV, slightly different from TWINS ($E_1 = 2.5$ and $E_2 = 97.5$ keV).

5.1. Ion Pressure Anisotropy

Ion pressure anisotropy is calculated as in Equation 2.

$$A = \frac{P_\perp - P_\parallel}{P_\parallel + P_\perp} \quad (2)$$

with

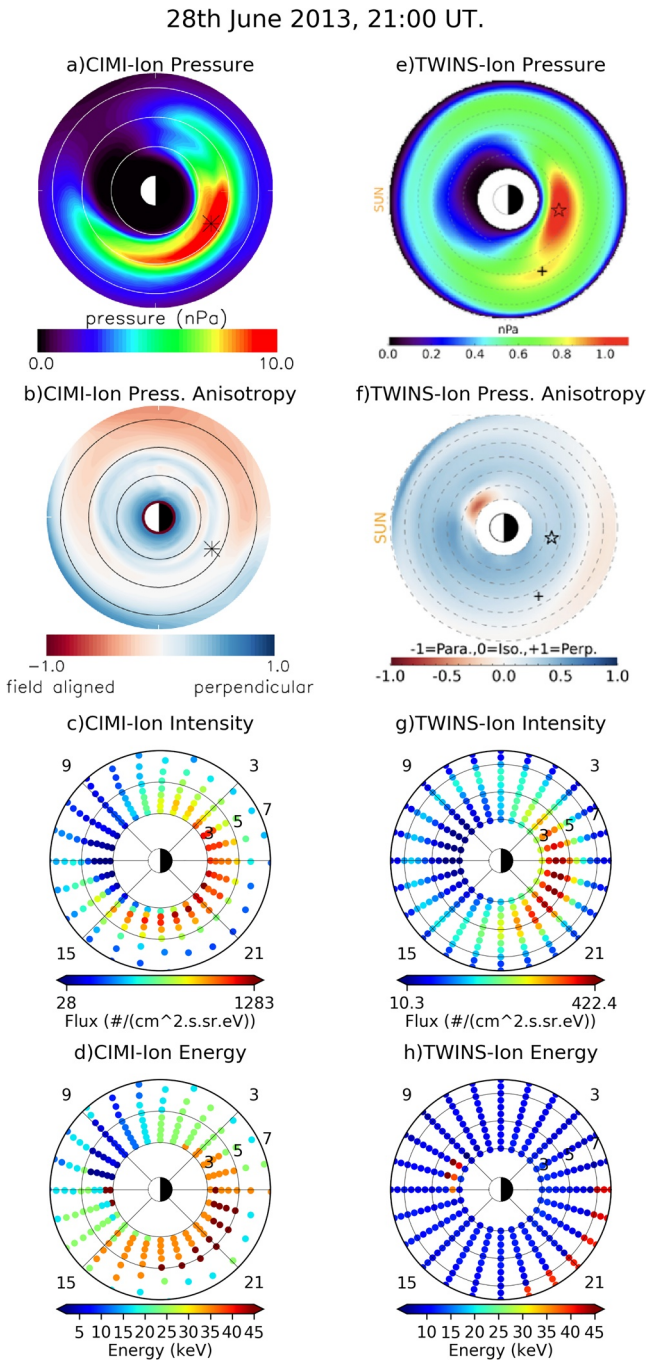

Figure 5. Same as Figure 4 at 21:00 UT on June 28, 2013. A secondary ion pressure peak in Two wide-angle Imaging Neutral-atom Spectrometers is marked as a black plus.

$$P_{\parallel} = 2\pi \int_{E_1}^{E_2} dE\sqrt{2mE} \int_{-1}^{1} F(E,n,cos\alpha)(dcos\alpha)sin^2\alpha$$

$$P_{\perp} = 2\pi \int_{E_1}^{E_2} dE\sqrt{2mE} \int_{-1}^{1} F(E,n,cos\alpha)(dcos\alpha)2cos^2\alpha$$

where symbols mean the same as Equation 1.

5.2. Ion Energy Spectra

TWINS ion spectra were obtained as explained in the last paragraph of Section 3. Figure 3 shows the energy resolution difference between TWINS and CIMI ion spectra. TWINS ion spectra is a smooth function since it is obtained through mathematical inversion. Even though both TWINS and CIMI have a global maxima at the same energy, TWINS observes another local maxima. In such cases where TWINS ion energy spectra had local energy maxima at multiple energies, we only consider the largest ion intensity peak at a given location and the energy at which the maxima was observed. These are referred to as ion intensity and ion energy, respectively, in Figures 4–10.

6. Observations

6.1. Comparisons at Specific Times

Each of Figures 4–10 show spatial profiles of ion pressure, anisotropy, intensity, and energy of the spectral peak from TWINS and CIMI simulations at specific times at which geomagnetic conditions showed fast or slow variations starting with the onset of the storm at 11:00 UT on June 28 to almost the end of the recovery phase at 23:00 UT on June 29.

6.1.1. 11:00 UT on June 28

At this time (marked as Figure 4 in Figure 1), IMF *Bz* gradually turned southward and IMF By had been negative for several hours. The AE index is flat indicating that there may not have been particle injections from the plasma sheet. Sym/H has gradually dropped to ~−10 nT and steeply dropped to lower values post 11:00 UT. Hence, this was the onset of the geomagnetic storm. Figures 4a and 4e show that TWINS ion pressure peak is shifted duskward in MLT and less than $1R_E$ further radially compared to CIMI.

Figures 4b and 4f show that a region of parallel pressure anisotropy is observed for radial distances $>6R_E$ on the midnight side for CIMI, whereas in TWINS data, perpendicular pressure anisotropy is observed at all locations. This band of parallel anisotropy on the nightside in the CIMI simulations may come from drift shell splitting. The drift shells of perpendicular ions follow the magnetic field iso-contours, so the drift shells are further away from the Earth on the dayside than on the night side. The drift shells of parallel ions are relatively circular. Therefore, the drift shells of perpendicular ions at $r > 6R_E$ on the nightside may encounter the magnetopause on the dayside, so ions are lost on the dayside. On the other hand, parallel ions drift to the dayside with similar distance inside the magnetopause and drift back to the nightside. Therefore, more parallel ions are found on the nightside at higher radial distances. In addition, at this time, flux/pressure is low and the anisotropy would easily go extreme in the simulation results, which might be the reason for the differences. Both CIMI and TWINS show perpendicular pressure

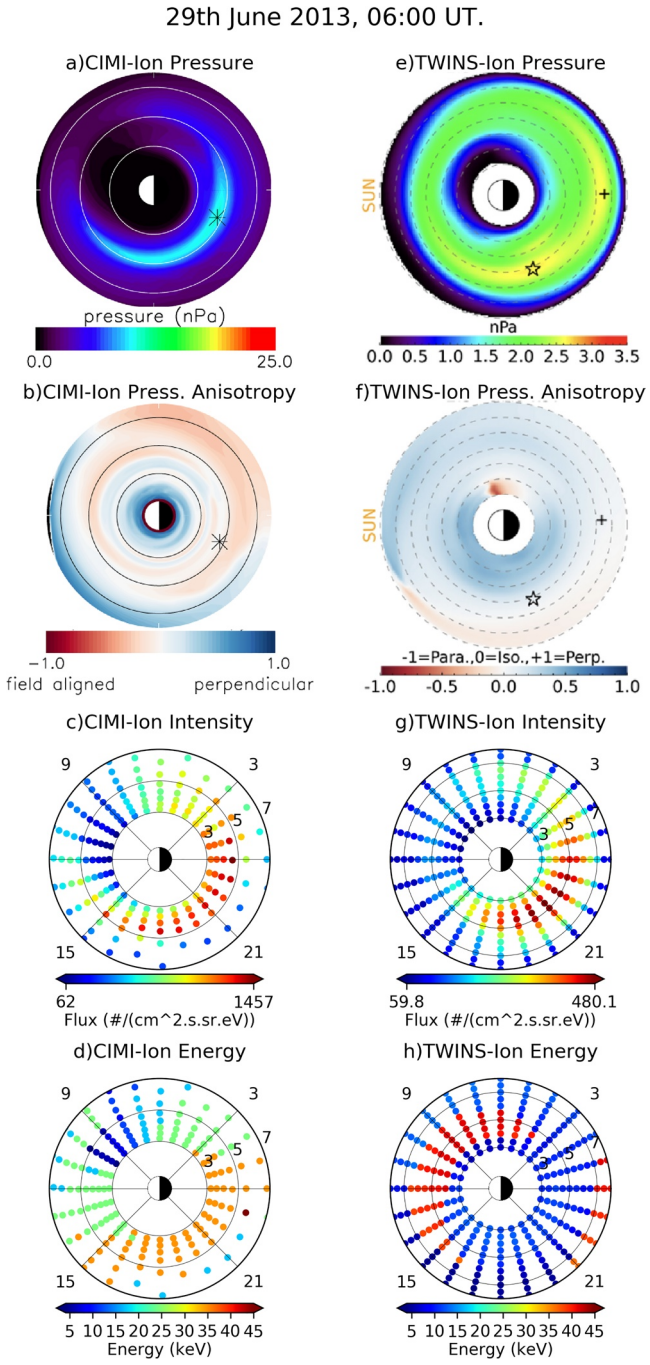

Figure 6. Same as Figure 4 at 06:00 UT on June 29, 2013. A secondary ion pressure peak in Two wide-angle Imaging Neutral-atom Spectrometers is marked as a black plus.

at the peak flux/pressure of the RC where the flux is large enough for better anisotropy calculations.

Figures 4c and 4g show the spatial distributions of maximum intensities of ions from CIMI and TWINS. Radially, TWINS data shows RC intensities between 4 and 7R_E whereas CIMI shows majority of it between 3 and 5R_E. They are located on the night side between MLT 6 and 18 h for TWINS and CIMI. The differences in the calculations of modeled ionospheric electric fields may produce these results as they shield the ions from penetrating deeper into the inner magnetosphere. We also found that when electron precipitation was not used to modify the convection potential calculation, the ions were found to penetrate deeper radially. This indicates that the inclusion of electron precipitation improved electric field shielding as the radial distributions of ions agree better with TWINS.

Figures 4d and 4h show the spatial distributions of energies at which ion spectra had maximum intensities from CIMI and TWINS. This distribution is representative of particle drift paths. For CIMI and TWINS, higher energy ions (>35 keV) are located on the noon side at lower radial distances, whereas ions with energies between 20 and 35 keV are located on the midnight side. This is expected as the solar wind parameter variations had been varying gradually for several hours conserving the first adiabatic invariant (μ).

6.1.2. 21:00 UT on June 28

At 21:00 UT on June 28 (marked as Figure 5 in Figure 1), the storm is in the main phase. IMF By is gradually recovering to near 0 values and Sym/H is dropping steeply to a minima at ∼−100 nT. IMF *Bz* has been steadily southward for several hours and AE index shows some fluctuations indicating substorm ion injections due to enhanced convection. Figures 5a and 5e show that that the two ion pressure peaks were observed for TWINS, whereas a single pressure peak was obtained in CIMI simulation results.

The regions of parallel anisotropy (Figures 5b and 5f) are located between 6 and 8R_E in both TWINS and CIMI but skewed toward the morning sector for CIMI. The differences in the observations may arise from the exclusion of ion injections in CIMI simulations and drift shell splitting as explained for 11:00 UT in the previous subsection. The region of parallel anisotropy near the midnight sector in TWINS indicates ion injections (Perez et al., 2018) which were not included in the CIMI simulations.

TWINS and CIMI ion intensity distributions are mostly located near 3–5 R_E and around the midnight sector (see Figures 5c and 5g). Figures 5d and 5h show that compared to CIMI where RC ion peaks are observed at 30–35 keV in the regions of maximum ion intensity, TWINS observed peaks at very low energies (∼<10 keV). Since TWINS measures energies using velocity measurements, very low energy peaks in the ion spectrum often indicate the presence of heavy ions. For example, 80 keV oxygen ions will be observed as 80 keV/16 amu = 5 keV/amu in TWINS ion spectrum. Hence, such low energies observed in TWINS ion spectra are often a result of O^+ ions (Valek et al., 2013; Shekhar et al., 2021) and may indicate convective transport from a plasma sheet abundant in oxygen.

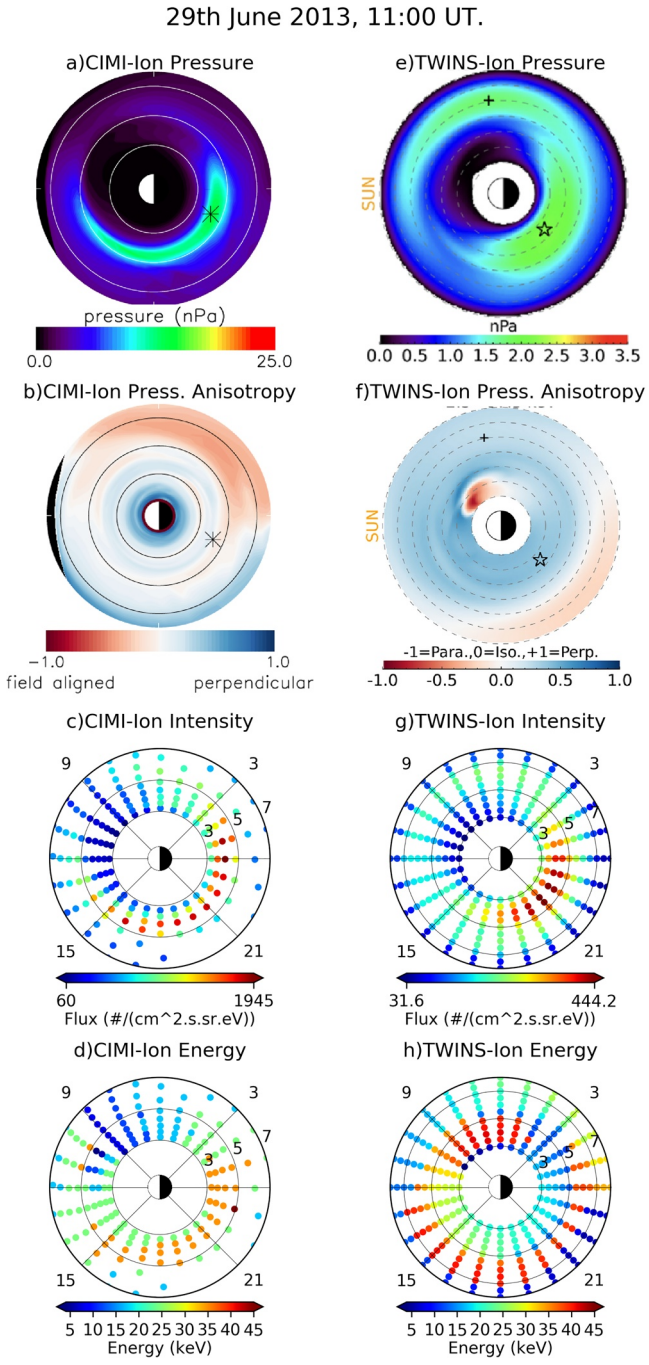

Figure 7. Same as Figure 4 at 11:00 UT on June 29, 2013. A secondary ion pressure peak in Two wide-angle Imaging Neutral-atom Spectrometers is marked as a black plus.

6.1.3. 6:00 UT on June 29

At 6:00 UT on June 29 (marked as Figure 6 in Figure 1), IMF *By* is positive and IMF *Bz* has been steadily southward for several hours. The storm is at about the minimum Sym/H and AE index is fluctuating rapidly. Figures 6a and 6e show that TWINS observes two ion pressure peaks while CIMI ion pressure profile is similar to the previous times with a single peak.

Further, Figures 6b and 6f indicate regions of parallel anisotropy in the dusk sectors at radial locations >5R_E in TWINS observations not observed in CIMI. The spatial profiles of maximum ion intensities are similar for TWINS and CIMI (Figures 6c and 6g), but TWINS RC energies are lower (<10 keV) compared to CIMI (~30 keV) as seen in Figures 6d and 6h. The low energy of ions from TWINS observations at times between 21:00 on June 28 and 06:00 UT on June 29, 2013 (see Figures 5 and 6h) indicate convective transport O^+ ions throughout the main phase of the storm.

6.1.4. 11:00 UT on June 29

IMF *By* is positive and IMF *Bz* has been steadily southward for several hours, it is well into the recovery phase and sharp spike in AE index is observed at 11:00 UT on June 29, indicating substorm particle injections (marked as Figure 7 in Figure 1). Figures 7a and 7e show that multiple ion pressure peaks are located in the TWINS pressure profile, whereas CIMI ion pressure profile has not varied much from previous observations. Figures 7b and 7f indicate regions of parallel anisotropy between 6 and 8R_E in the pre-midnight sector in TWINS observations not observed in CIMI. This is expected since the simulations do not account for particle injections. The ion intensities in Figures 7c and 7g are similar for TWINS and CIMI. The spatial profiles of ion peak energies shown in Figures 7d and 7g are very different for TWINS and CIMI. This is expected as the timescales of particle injections may have violated the first adiabatic invariant, whereas CIMI simulations conserve the first adiabatic invariant. The ion energies at RC peak intensities is ~15–20 keV for TWINS whereas it is ~30–35 keV for CIMI. Since, the ion energies for TWINS are still <25 keV, it may imply an abundance of O^+ ions (Shekhar et al., 2021).

6.1.5. 14:00 UT on June 29

At 14:00 UT on June 29 (marked as Figure 8 in Figure 1) is an interesting time as this is 1 h after IMF *Bz* rapidly turned northward again and IMF By was at its peak (~10 nT). Also, it is about 3 h from the large jump in AE observed at 11:00 UT. Figures 8a and 8e show that CIMI and TWINS seem to agree with the peak in the dusk/midnight sector at about 4R_E, but TWINS sees another larger peak near noon at ~6.5R_E. This could be due to the fact that the input to CIMI, plasma sheet density changes relatively slowly compared to solar wind density (Figure 1, fourth and seventh panel). Figures 8b and 8f show that both TWINS and CIMI pressures have perpendicular anisotropy at pressure peaks. Since IMF *Bz* rapidly turned northward here, shielding electric fields may have contributed to the differences between CIMI and TWINS ion pressure peaks. Further, high positive values of IMF By skew the high-latitude ionospheric potential pattern (Weimer, 1995) and may have contributed to the observed shift in the TWINS ion pressure peak. Spatial profiles of the maximum ion intensities from TWINS and CIMI are similar (Figures 8c and 8g). The spatial profiles of ion energies at spectral peaks differ (Figures 8d and 8h). CIMI simulations show the partial RC consisting of ions ~30 keV whereas in TWINS, ions in the pre-midnight and midnight sector

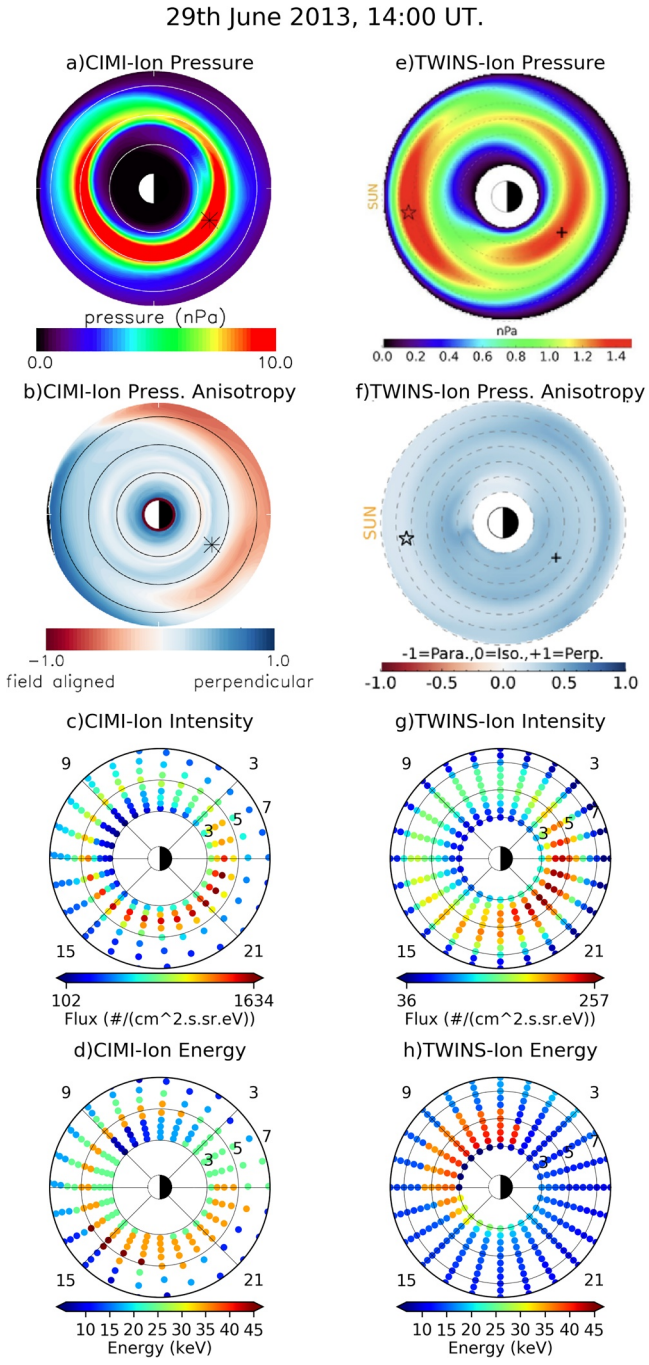

Figure 8. Same as Figure 4 at 14:00 UT on June 29, 2013. A secondary ion pressure peak in Two wide-angle Imaging Neutral-atom Spectrometers is marked as a black plus.

(where ion intensities peak) have energies ~5–25 keV. This could be due to the presence of heavy ions.

6.1.6. 18:00 UT on June 29

Around 18:00 UT on June 29 (marked as Figure 9 in Figure 1), Sym/H has recovered to ~50 nT, AE index is flat and it is almost 12 h into the recovery phase of the storm. TWINS observations show that the ion pressure is more ring-like and has single pressure peak in agreement with CIMI (Figures 9a and 9e). However, CIMI pressure profile seems to be radially compressed relative to TWINS. Figures 9b and 9f indicate bands of parallel anisotropy between 6 and 8R_E around midnight sector in CIMI not observed in TWINS observations which has been a constant feature in the CIMI simulations at all times attributed to drift shell splitting. Both TWINS and CIMI pressures are nearly isotropic at pressure peaks (Figures 8b and 8f). The spatial distributions of maximum intensities of ions from TWINS and CIMI show that the RC has moved away radially compared to 14:00 UT (Compare Figures 8c and 9c; 8g and 9g). This could be due to changing ionospheric electric field patterns as convection rates slow down.

The spatial profiles of ion peak energies (Figures 9d and 9h) are different for TWINS and CIMI. For TWINS, the low energy ions seem to arrange themselves in the pre-midnight sector whereas higher energy ions arrange themselves in the post-midnight sector. Since geomagnetic activity has calmed down around 14:00 UT on June 29, it is expected as the RC is mostly composed of ions that have been drifting for a few hours. As H^+ ions (where ion energies ~30 keV) drift faster than O^+ ions (where ion energies ~10 keV), they may have been able to drift from midnight-noon-post midnight sectors faster resulting in the observed distribution in Figure 9h. In the CIMI simulations, RCs are assumed to be only composed of H^+ ions, which are getting energized as they drift from midnight to post noon sectors and thrown out of drift orbit as the gyroradius gets larger due to energization (Figure 9d).

6.1.7. 23:00 UT on June 29

At 23:00 UT on June 29 (marked as Figure 10 in Figure 1), the recovery phase continues with no rapid variations in the AE index for several hours prior indicating no particle injections. In Figures 10a and 10e, it can be seen that TWINS pressure peak is located radially outward compared to CIMI.This could be a result of differences in the modeled and observed shielding electric fields. At the ion pressure peak, nearly isotropic pressure is observed for TWINS and CIMI (Figures 10b and 10f). The peak ion intensity profile is similar but radially expanded in TWINS compared to CIMI as seen in Figures 9g and 10c.

The spatial profiles of ion energies at spectral peak show a partial RC comprising of 25–45 keV ions in CIMI simulations whereas 35–40 keV ions in TWINS (Figures 10d and 10h). It is also interesting that most of the O^+ ions, represented by ion energies <10 keV, have been scattered out in Figure 10h. This is expected as at this time, RCs mostly comprise of remnant ions drifting for a few hours and since O^+ ions will have larger gyroradii, it is likely that they will scatter before the H^+ ions.

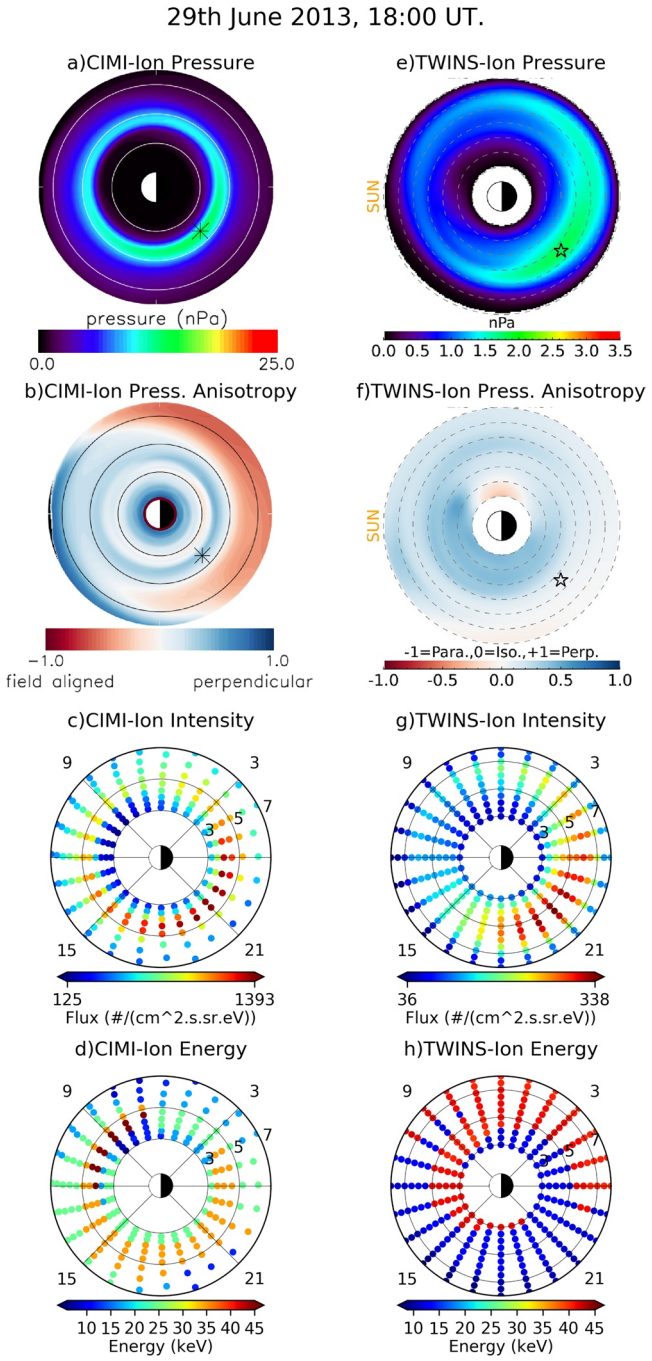

Figure 9. Same as Figure 4 at 18:00 UT on June 29, 2013.

6.2. Variations in Ion Pressure Peaks

Figure 11 shows the radial (top plot) and MLT (bottom plot) variations in the ion pressure peak locations for June 28 and 29, 2013. The largest peaks in the ion pressure profiles at each hour are referred to as primary peaks whereas the second largest peaks are referred to as secondary peaks. The times at which detailed observations were made are marked and correspond to the times marked in Figure 1. TWINS observed multiple ion pressure peaks between 21:00 UT on June 28, a few hours after IMF *Bz* turned southward to 15:00 UT on June 29, a few hours after IMF *Bz* turned northward. This was also the period when AE index showed several short-duration fluctuations. Further, CIMI simulations were unable to capture multiple ion pressure peaks.

Radially, CIMI ion pressure peaks show less variability than TWINS. Comparisons between Figure 11 top plot and Figure 1 show that as IMF *Bz* gradually turned southward between 09:00 and 18:00 UT on June 28, CIMI ion pressure peaks moved closer from $5.5R_E$ to $4R_E$, while in the recovery phase starting at 06:00 UT on June 29, remained around $4R_E$. TWINS ion pressure peaks show a similar trend until almost the end of recovery phase at 16:00 UT on June 29, after which ion pressure peaks are located around $6R_E$.

From the time of the main phase of the storm (~12:00 UT June 28), there is less variability and good agreement in the MLT locations of the ion pressure peaks in TWINS observations and CIMI simulations (Figure 11 bottom plot). For times before the onset of the storm, comparisons of Figure 11 bottom plot with solar wind data (Figure 1) shows that between 02:00 and 03:00 UT on June 28, 2013, when IMF By rapidly changed direction from positive to negative and IMF *Bz* turned northward, MLT location of ion pressure peak was observed to shift eastward in TWINS data. In contrast, CIMI obtained locations of ion pressure peaks did not vary much and stayed mostly around pre-midnight to midnight sectors which could be due to the fact that compared to solar wind density, input from the plasma sheet density is relatively smooth.

Between 13:00 and 14:00 UT on June 29 (Figure 11 bottom plot), TWINS ion pressure peaks are seen to be shifted westward to almost noon. As seen in Figure 8e, at 14:00 UT, TWINS observed two ion pressure peaks with the primary peak in the noon sector and a secondary peak around pre-midnight closer to the MLT location observed by CIMI. It is to be noted that IMF By at this time rapidly jumped to values >5 nT. It is known that high positive values of IMF By skew the high-latitude ionospheric potential pattern (Weimer, 1995). However, the role of IMF By in the skewing of the ion pressure peak is still an open question and while it may have led to the observed noon skewing of TWINS ion pressure peak post 13:00 UT on June 29, 2013, more work is needed to explore these phenomena.

7. Discussions and Conclusions

In this study, we simulated a geomagnetic storm (SymH ~−100 nT) from June 28 to 29, 2013 using the CIMI CRCM model and compared the results with TWINS observations of global ion pressure, anisotropy, intensity and ion energies at spectral peaks. In general, the CIMI pressure and flux are about one order of magnitude higher than those from TWINS. Further, during geomagnetically quiet times, spatial profiles of TWINS

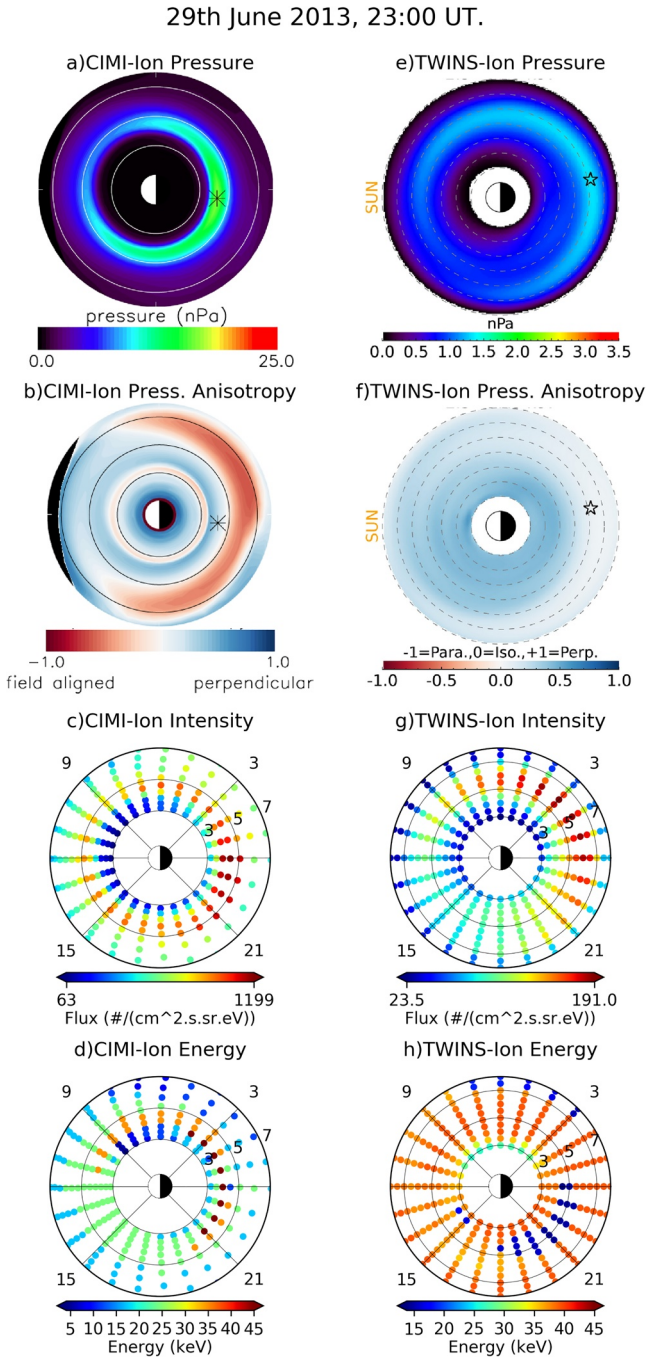

Figure 10. Same as Figure 4 at 23:00 UT on June 29, 2013.

ion intensities and ion energies at spectral peak are radially expanded compared to CIMI simulations. During the times of enhanced convection and rapid AE index fluctuations, indicating substorm injections, TWINS observed two ion pressure peaks whereas CIMI observed only one ion pressure peak. Further, regions of parallel pressure anisotropy were observed near pre-midnight at most of these times in TWINS data but absent in CIMI simulations. Since CIMI simulations did not include ion injections, it could be concluded that multiple ion pressure peaks and parallel ion anisotropies in TWINS data were correlated with ion injections. This is also in agreement with results from Perez et al. (2015) and Perez et al. (2018), where multiple TWINS ion pressure peaks were found to be associated with particle injections.

The convection electric field transporting the particles from the plasma sheet to the magnetosphere map along open field lines in the polar ionosphere. The radial current density at the ionosphere can be determined from the equatorial pressure (Heinemann, 1990). The azimuthal shifts in the ion pressure peaks represent the variations in the Birkeland region 2 currents which are field-aligned currents coupling the magnetosphere to the ionosphere. Most of the field-aligned current closure takes place through local Pedersen currents within the auroral zone flowing between the upward and downward Birkeland region 1 and region 2 currents. During geomagnetic storms, when IMF *Bz* turns northward rapidly, the electric fields in the ionosphere can shield the ions from penetrating further into the inner magnetosphere (Perez et al., 2018). The RC can also be influenced by the morphological features of the auroral electron precipitation and solar radiation (Ebihara et al., 2004). Before the onset of the storm, between 08:00 and 11:00 UT on June 28, and way into the recovery phase after 18:00 UT on June 29, Figure 11 top plot shows that ion pressure peaks were located radially further in TWINS observations compared to CIMI. Comparison between Figures 8c and 8g; 9c and 9g, show that the ion intensities radially expanded for CIMI and TWINS but more prominently in TWINS. This could be due to the variations in IMF *Bz* rapidly turning northward (see Figure 1) affecting the shielding electric fields which in turn could shield the ions from penetrating further into the inner magnetosphere. However, between 11:00 and 21:00 UT on June 28, TWINS observed ion intensities radially contracting (Figures 4 and 5g), whereas CIMI ion intensities do not follow a similar trend (Figures 4c and 5c). Geomagnetic conditions are quiet at 11:00 UT on June 28 and AE index is observed to be flat (see Figure 1). Since shielding electric fields are influenced by several factors other than solar wind conditions, CIMI modeled electric fields may not have captured this feature.

Figure 11 bottom plot and Figure 1 show that between 02:00 and 03:00 UT on June 28, IMF *Bz* rapidly turned northward causing a westward (post-midnight) shift in the location of TWINS RC ion pressure peak which remained for ~2 h. Further, at 13:00 UT IMF *By* is ~10 nT and IMF *Bz* rapidly jumps to 0. At these times, TWINS observed skewing of the RC ion pressure peak to almost noon lasting for ~4 h. The CIMI RC ion pressure peaks were located in the pre-midnight sector throughout the storm. This indicates that shielding electric fields and/or twisting of the convection due to large IMF *By* (Cson Brandt et al., 2002; Weimer, 1995) may have led to the observed azimuthal shifts in the TWINS RC ion pressure peaks.

Spatial distributions of energies at which ion intensities peaked showed that during slow variation of solar wind parameters ion drift patterns between TWINS and CIMI agreed well as seen at 11:00 UT on June 28

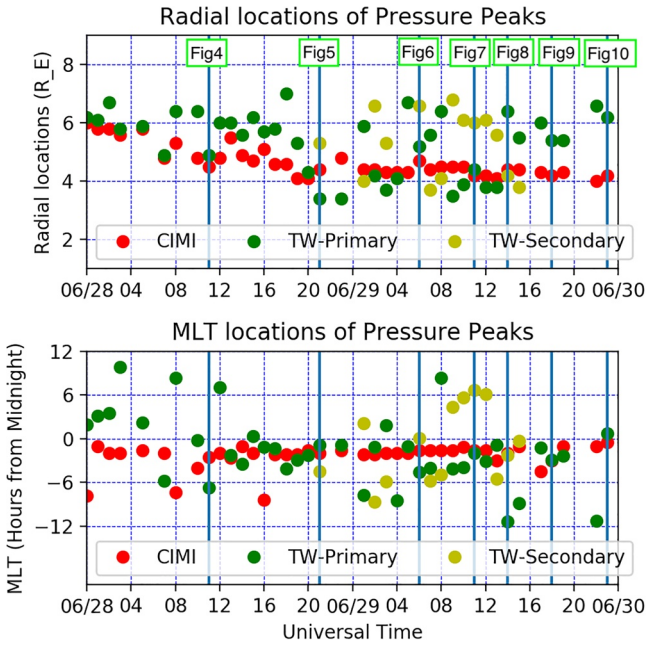

Figure 11. Top: Radial locations of ion pressure peaks are plotted versus time from 00:00 UT on June 28, 2013 to 00:00 UT on June 30, 2013 for Comprehensive Inner Magnetosphere-Ionosphere (CIMI) and Two wide-angle Imaging Neutral-atom Spectrometers (TWINS). Bottom: MLT locations of ion pressure peaks are plotted versus time from 00:00 UT on June 28, 2013 to 00:00 UT on June 30, 2013 for CIMI and TWINS. The times where detailed analyses are described in Section 6.1 are marked as blue vertical lines. TW—Primary shows the locations of the largest ion pressure peak and TW—Secondary shows the locations of the second-largest ion pressure peak in TWINS data.

(Figures 4d and 4h). This is expected as CIMI traces ion drift paths with the assumption that the first adiabatic invariant (μ) is conserved which will hold true when variations are slow. Between 21:00 UT on June 28 and 06:00 UT on June 29, TWINS RC consisted of ions with energies < 10 keV (Figures 5 and 6h) and TWINS RC intensities peak at lower radial distances compared to 11:00 UT on June 28 when these low energy ions were not observed in TWINS (compare Figures 4 and 5g). These low energy ions penetrating deeper into the magnetosphere suggest an abundance of O^+ ions due to their transport either from the plasma sheet or the ionosphere as they will be trapped at lower radial distances (Shekhar et al., 2021). Further, solar wind data indicate that this encompassed the main phase of the storm (see Figure 1) and previous studies have shown that O^+ ions are more likely to be abundant during the main phase (Daglis, 1996; Greenspan & Hamilton, 2002; Hamilton et al., 1988; Valek et al., 2015). This might explain why TWINS observed ions at such low energies since it does not differentiate between ion species. Even though H^+ and O^+ ENAs can be separated, they cannot be deconvolved with the current tools available (Perez et al., 2012; Valek et al., 2013). At the highest AE peak (2,500 nT) at 11:00 UT on June 29, TWINS RC consists of ions with energies ~15–25 keV whereas CIMI RC consists of ions with energies ~30–35 keV (Figures 7d and 7h). Also, ions from substorm injections begin to fill into the dusk-midnight-early morning sectors and CIMI and TWINS drift patterns are completely different. This is expected as particle injections will violate the conservation of μ. Note that ion energies in TWINS are <25 keV and so the RC may still be abundant in O^+ ions (Shekhar et al., 2021). From 18:00 to 23:00 UT, TWINS and CIMI RC mostly comprise of remnant ions drifting for a few hours. As such, TWINS gradually observed reduction of low energy ions implying that O^+ ions might be getting scattered before H^+ ions as they will have a larger gyroradius. CIMI observed partial RC initially distributed in the midnight-dusk-noon sector drifting to post noon-morning-midnight sector indicating drifting trapped ions.

TWINS and CIMI results were found to agree on the general features of the RC. However, the effects of shielding electric fields appear to be underestimated in CIMI simulations during quiet times. The presence of O^+ ions and particle injections were prominent in TWINS observations but did not appear in CIMI simulations. This was expected as CIMI simulations assume RC to be composed of only H^+ ions and do not include ion injections. While previous studies such as those by Perez et al. (2018) have found similar results through comparison with simulations, in this study, we also investigated the spatial profiles of ion peak energies which are associated with particle drift paths. This allowed us to directly compare drift patterns of ions from TWINS with CIMI, which had not been explored before. In future, it would be interesting to examine such comparisons for more geomagnetic storms with inclusions of particle injections in the CIMI model so that global RC dynamics can be understood better.

Data Availability Statement

TWINS data are accessible from the Coordinated Data Analysis Web (CDAWeb) (https://cdaweb.gsfc.nasa.gov). All simulations in this study were performed on the Auburn University High Performance and Parallel Computing Facility (https://hpc.auburn.edu/hpc/index.php). The CIMI simulation data are available for download at http://doi.org/10.5281/zenodo.5047408.

Acknowledgments
This study was supported by the TWINS mission, a part of NASA's Explorer Program. The authors are thankful to ACE and Wind plasma and magnetometer teams for L1 data and OMNI for providing availability of the data set at omniweb.gsfc.nasa.gov.

References

Anderson, B. J., Ohtani, S. I., Korth, H., & Ukhorskiy, A. (2005). Storm time dawn-dusk asymmetry of the large-scale Birkeland currents. *Journal of Geophysical Research*, *110*, A12220. https://doi.org/10.1029/2005JA011246

Angelopoulos, V., Temerin, M., Roth, I., Mozer, F. S., Weimer, D., & Hairston, M. R. (2002). Testing global storm-time electric field models using particle spectra on multiple spacecraft. *Journal of Geophysical Research*, *107*, SMP21-1–SMP21-11. https://doi.org/10.1029/2001JA900174

Bazell, D., Roelof, E. C., Sotirelis, T., Brandt, P. C., Nair, H., Valek, P., et al. (2010). Comparison of TWINS images of low-altitude emission of energetic neutral atoms with DMSP precipitating ion fluxes. *Journal of Geophysical Research*, *115*, A10204. https://doi.org/10.1029/2010JA015644

Borovsky, J. E., Thomsen, M. F., & Elphic, R. C. (1998). The driving of the plasma sheet by the solar wind. *Journal of Geophysical Research*, *103*, 17617–17639. https://doi.org/10.1029/97ja02986

Buzulukova, N., Fok, M. C., Goldstein, J., Valek, P., McComas, D. J., & Brandt, P. C. (2010). Ring current dynamics in moderate and strong storms: Comparative analysis of TWINS and IMAGE/HENA data with the comprehensive ring current model. *Journal of Geophysical Research*, *115*, A12234. https://doi.org/10.1029/2010JA015292

Carlson, C. W., Mcfadden, J. P., Turin, P., Curtis, D. W., & Magoncelli, A. (2001). The electron and ion plasma experiment for FAST, *Space Science Reviews*, *98*, 33–66. https://doi.org/10.1023/A:1013139910140

Cson Brandt, P., Ohtani, S., Mitchell, D. G., Fok, M.-C., Roelof, E. C., & Demajistre, R. (2002). Global ENA observations of the storm main phase ring current: Implications for skewed electric fields in the inner magnetosphere. *Geophysical Research Letters*, *29*, 1954. https://doi.org/10.1029/2002gl015160

Daglis, I. A. (1996). The role of magnetosphere-ionosphere coupling in magnetic storm dynamics. *Geophysical Monograph Series*, *98*, 107–116. https://doi.org/10.1029/GM098p0107

De Michelis, P., Daglis, I. A., & Consolini, G. (1999). An average image of proton plasma pressure and of current systems in the equatorial plane derived from AMPTE/CCE-CHEM measurements. *Journal of Geophysical Research: Space Physics*, *104*, 28615–28624. https://doi.org/10.1029/1999ja900310

Ebihara, Y., & Ejiri, M. (2000). Simulation study on fundamental properties of the storm-time ring current. *Journal of Geophysical Research: Space Physics*, *105*, 15843–15859. https://doi.org/10.1029/1999ja900493

Ebihara, Y., Ejiri, M., Nilsson, H., Sandahl, I., Grande, M., Fennell, J. F., et al. (2004). Multiple discrete-energy ion features in the inner magnetosphere: 9 February 1998, event. *Annales Geophysicae*, *22*, 1297–1304. https://doi.org/10.5194/angeo-22-1297-2004

Ebihara, Y., Ejiri, M., Nilsson, H., Sandahl, I., Milillo, A., Grande, M., et al. (2002). Statistical distribution of the storm-time proton ring current: POLAR measurements. *Geophysical Research Letters*, *29*, 1969. https://doi.org/10.1029/2002GL015430

Elfritz, J. G., Keesee, A. M., Buzulukova, N., Fok, M. C., & Scime, E. E. (2014). First results using TWINS-derived ion temperature boundary conditions in CRCM. *Journal of Geophysical Research: Space Physics*, *119*, 3345–3361. https://doi.org/10.1002/2013JA019555

Fok, M. C., Buzulukova, N., Chen, S. H., Valek, P. W., Goldstein, J., & McComas, D. J. (2010). Simulation and TWINS observations of the 22 July 2009 storm. *Journal of Geophysical Research*, *115*, A12231. https://doi.org/10.1029/2010JA015443

Fok, M. C., Buzulukova, N. Y., Chen, S. H., Glocer, A., Nagai, T., Valek, P., & Perez, J. D. (2014). The comprehensive inner magnetosphere-ionosphere model. *Journal of Geophysical Research: Space Physics*, *119*, 7522–7540. https://doi.org/10.1002/2014JA020239

Fok, M. C., Horne, R. B., Meredith, N. P., & Glauert, S. A. (2008). Radiation belt environment model: Application to space weather nowcasting. *Journal of Geophysical Research*, *113*, A03S08. https://doi.org/10.1029/2007JA012558

Fok, M. C., Moore, T. E., Wilson, G. R., Perez, J. D., Zhang, X. X., Son Brandt, P. C., et al. (2003). Global ENA image simulations. *Space Science Reviews*, *109*, 77–103. https://doi.org/10.1023/B:SPAC.0000007514.56380.fd

Fok, M. C., Wolf, R. A., Spiro, R. W., & Moore, T. E. (2001). Comprehensive computational model of Earth's ring current. *Journal of Geophysical Research*, *106*, 8417–8424. https://doi.org/10.1029/2000ja000235

Gloeckler, G., Wilken, B., Stüdemann, W., Ipavich, F. M., Hovestadt, D., Hamilton, D. C., & Kremser, G. (1985). First composition measurement of the bulk of the storm-time ring current (1 to 300 keV/e) with AMPTE-CCE. *Geophysical Research Letters*, *12*, 325–328. https://doi.org/10.1029/GL012i005p00325

Goldstein, J., & McComas, D. J. (2013). Five years of stereo magnetospheric imaging by TWINS. *Space Science Reviews*, *180*, 39–70. https://doi.org/10.1007/s11214-013-0012-8

Greenspan, M. E., & Hamilton, D. C. (2002). Relative contributions of H^+ and O^+ to the ring current energy near magnetic storm maximum. *Journal of Geophysical Research*, *107*, SMP3-1–SMP3-9. https://doi.org/10.1029/2001JA000155

Hamilton, D. C., Gloeckler, G., Ipavich, F. M., Stüdemann, W., Wilken, B., & Kremser, G. (1988). Ring current development during the great geomagnetic storm of February 1986. *Journal of Geophysical Research*, *93*, 14343–14355. https://doi.org/10.1029/ja093ia12p14343

Hardy, D. A., Gussenhoven, M. S., Raistrick, R., & McNeil, W. J. (1987). Statistical and functional representations of the pattern of auroral energy flux, number flux, and conductivity. *Journal of Geophysical Research*, *92*, 12275. https://doi.org/10.1029/ja092ia11p12275

Harel, M., Wolf, R. A., Reiff, P. H., Spiro, R. W., Burke, W. J., Rich, F. J., & Smiddy, M. (1981). Quantitative simulation of a magnetospheric substorm 1. Model logic and overview. *Journal of Geophysical Research*, *86*, 2217. https://doi.org/10.1029/ja086ia04p02217

Heinemann, M. (1990). Representations of currents and magnetic fields in anisotropic magnetohydrostatic plasma. *Journal of Geophysical Research*, *95*, 7789. https://doi.org/10.1029/ja095ia06p07789

Jorgensen, A. M., Spence, H. E., Hughes, W. J., & Singer, H. J. (2004). A statistical study of the global structure of the ring current. *Journal of Geophysical Research*, *109*, A12204. https://doi.org/10.1029/2003JA010090

Kistler, L. M., Klecker, B., Jordanova, V. K., Möbius, E., Popecki, M. A., Patel, D., et al. (1999). Testing electric field models using ring current ion energy spectra from the Equator-S ion composition (ESIC) instrument. *Annales Geophysicae*, *17*, 1611–1621. https://doi.org/10.1007/s00585-999-1611-2

Kistler, L. M., & Larson, D. J. (2000). Testing electric and magnetic field models of the storm-time inner magnetosphere. *Journal of Geophysical Research*, *105*, 25221–25231. https://doi.org/10.1029/2000ja000132

Le, G., Russell, C. T., & Takahashi, K. (2004). Morphology of the ring current derived from magnetic field observations. *Annales Geophysicae*, *22*, 1267–1295. https://doi.org/10.5194/angeo-22-1267-2004

McComas, D. J., Allegrini, F., Baldonado, J., Blake, B., Brandt, P. C., Burch, J., et al. (2009). The two wide-angle imaging neutral-atom spectrometers (TWINS) NASA mission-of-opportunity. *Space Science Reviews*, *142*, 157–231. https://doi.org/10.1007/s11214-008-9467-4

McComas, D. J., Buzulukova, N., Connors, M. G., Dayeh, M. A., Goldstein, J., Funsten, H. O., et al. (2012). Two wide-angle imaging neutral-atom spectrometers and interstellar boundary explorer energetic neutral atom imaging of the 5 April 2010 substorm. *Journal of Geophysical Research*, *117*, A03225. https://doi.org/10.1029/2011JA017273

Perez, J. D., Edmond, J., Hill, S., Xu, H., Buzulukova, N., Fok, M. C., et al. (2018). Dynamics of a geomagnetic storm on 7–10 September 2015 as observed by TWINS and simulated by CIMI. *Annales Geophysicae*, *36*, 1439–1456. https://doi.org/10.5194/angeo-36-1439-2018

Perez, J. D., Goldstein, J., McComas, D. J., Valek, P., Buzulukova, N., Fok, M. C., & Singer, H. J. (2015). TWINS stereoscopic imaging of multiple peaks in the ring current. *Journal of Geophysical Research: Space Physics*, *120*, 368–383. https://doi.org/10.1002/2014JA020662

Perez, J. D., Grimes, E. W., Goldstein, J., McComas, D. J., Valek, P., & Billor, N. (2012). Evolution of CIR storm on 22 July 2009. *Journal of Geophysical Research*, *117*, A09221. https://doi.org/10.1029/2012JA017572

R, J., & de Boor, C. (1980). A practical guide to splines. In: In A. Wigderson (Ed.), *Mathematics of Computation* (Vol. 27). Princeton University Press. https://doi.org/10.2307/2006241

Scudder, J., Hunsacker, F., Miller, G., Lobell, J., Zawistowski, T., Ogilvie, K., et al. (1995). Hydra—A 3-dimensional electron and ion hot plasma instrument for the POLAR spacecraft of the GGS mission. *Space Science Reviews*, *71*, 459–495. https://doi.org/10.1007/BF00751338

Shekhar, S., Perez, J. D., & Ferradas, C. P. (2021). TWINS observations of the dynamics of ring currents ion spectra on March 17 and October 7, 2015. *Journal of Geophysical Research: Space Physics*, *126*(2), e2020JA028156. https://doi.org/10.1029/2020ja028156

Shi, Y., Zesta, E., Lyons, L. R., Yumoto, K., & Kitamura, K. (2006). Statistical study of effect of solar wind dynamic pressure enhancements on dawn-to-dusk ring current asymmetry. *Journal of Geophysical Research*, *111*, A10216. https://doi.org/10.1029/2005JA011532

Stern, D. P. (1975). The motion of a proton in the equatorial magnetosphere. *Journal of Geophysical Research*, *80*, 595–599. https://doi.org/10.1029/ja080i004p00595

Tsyganenko, N. A. (1989). A magnetospheric magnetic field model with a warped tail current sheet. *Planetary and Space Science*, *37*, 5–20. https://doi.org/10.1016/0032-0633(89)90066-4

Valek, P. W., Goldstein, J., Jahn, J. M., McComas, D. J., & Spence, H. E. (2015). First joint in situ and global observations of the medium-energy oxygen and hydrogen in the inner magnetosphere. *Journal of Geophysical Research: Space Physics*, *120*, 7615–7628. https://doi.org/10.1002/2015JA021151

Valek, P. W., Goldstein, J., McComas, D. J., Iiie, R., Buzulukova, N., Fok, M. C., & Perez, J. D. (2013). Oxygen-hydrogen differentiated observations from TWINS: The 22 July 2009 storm. *Journal of Geophysical Research: Space Physics*, *118*, 3377–3393. https://doi.org/10.1002/jgra.50204

Volland, H. (1973). A semiempirical model of large-scale magnetospheric electric fields. *Journal of Geophysical Research*, *78*, 171–180. https://doi.org/10.1029/ja078i001p00171

Wahba, G. (1990). *Spline models for observational data*. Society for Industrial and Applied Mathematics. https://doi.org/10.1137/1.9781611970128

Weimer, D. R. (1995). Models of high-latitude electric potentials derived with a least error fit of spherical harmonic coefficients. *Journal of Geophysical Research*, *100*, 19595. https://doi.org/10.1029/95ja01755

Weimer, D. R. (1996). A flexible, IMF dependent model of high-latitude electric potentials having "space weather" applications. *Geophysical Research Letters*, *23*, 2549–2552. https://doi.org/10.1029/96GL02255